

UNIVERSIDAD DE LOS ANDES
FACULTAD DE INGENIERÍA Y CIENCIAS APLICADAS



TÍTULO TESIS

LUKAS WOLFF CASANOVA

TESIS PARA OPTAR AL GRADO DE
MAGÍSTER EN CIENCIAS DE LA INGENIERÍA

PROFESOR GUÍA: PATRICIO MORENO

PROFESOR Co-GUÍA: ALVARO PAUL

PROFESOR Co-GUÍA: JORGE GOMEZ

SANTIAGO, AGOSTO DE 2023

Devotion

Abstract

Acknowledgements

Contents

Devotion	iii
Abstract	iv
Acknowledgements	v
1 Introduction	1
1.1 Hypothesis	3
1.2 Objectives	3
1.2.1 General Objective	3
1.3 Specific Objectives	4
1.4 Thesis Structure	4
2 Bibliographic Revision	5
2.1 Multiphase Flow Simulation	6
2.1.1 Fluid Phase (CFD)	6
2.1.2 Fiber Phase (DEM)	7
2.1.3 Phases Coupling (CFD-DEM)	9
2.2 Particle Image Velocimetry	10
2.3 Particle Tracking Velocimetry	11
2.3.1 Particle Detection	12
2.3.2 Particle Correlation	13
3 Methodology	15
3.1 Particle Tracking Velocimetry Implementation	15
Nomenclature	18
References	19

List of Figures

2.1	L-shape model for UHPC flow analysis	5
2.2	Rheological properties of Carbopol at different concentrations	6
2.3	Example of a CFD computational domain, with two mesh types: tetrahedrons and hexahedrons.	8
2.4	PIV setup based on the L-Shape model	11
2.5	PTV setup based on volumetric illumination	12
3.1	PTV flowchart	15
3.2	Examples of fiber light reflection: (i) a group of fibers with suboptimal alignment relative to the light source, (ii) a well-illuminated fiber, and (iii) a fiber exhibiting non-uniform light reflection along its length.	16
3.3	Representative examples from the training dataset: (a) image with a low concentration of well-separated fibers; (b) image with a high concentration of overlapping fibers and a significant presence of bubbles.	17

List of Tables

Chapter 1

Introduction

Concrete is ubiquitous: it can be found in every house, town, city, and country, regardless of the level of development, wealth, or political foundation of the region. It is such a versatile material—initially fluid, but hardening over time into a rock-like solid—that it can be used in countless applications, from the foundation of a small house to the construction of bridges and skyscrapers. Concrete is composed of three main components: cement, water, and aggregates (such as sand, gravel, or stone). Together, these elements constitute the most widely used construction material worldwide, with global demand projected to increase by approximately 12% - 23% by 2050 (Cheng, Reiner, Yang, Cui, Meng, Shan, Liu, Tao & Guan, 2023).

Cement production alone is responsible for 8% of global CO_2 emissions (Winnefeld, Leemann, German & Lothenbach, 2022). When the water demand and the emissions from construction activities are also considered, it becomes clear that concrete production accounts for a significant percentage of annual CO_2 emissions worldwide. For this reason, several restrictions and sustainable practices are being adopted, such as the use of recycled aggregates or alternative cementitious materials (e.g., fly ash, slag, or silica fume), which reduce the amount of cement required in concrete production and extend the service life of structures.

Concrete exhibits excellent compressive strength (around 30 MPa) but relatively poor tensile strength (around 3 MPa). To overcome this limitation, steel reinforcement is commonly used to enhance tensile resistance. However, reinforcement introduces durability issues, as steel is prone to corrosion. Chlorides can penetrate the porous structure and microcracks of the concrete, leading to steel corrosion, a reduction in

structural integrity, and increased maintenance costs.

Ultra-High-Performance Concrete (UHPC) has been developed to address these challenges, with the aim of improving durability and extending the lifespan of concrete structures. UHPC is characterized by very high compressive strength (around 150 MPa), extremely low permeability, and excellent resistance to environmental factors such as freeze-thaw cycles and chemical attack. These properties are achieved by incorporating high-quality materials such as silica fume, superplasticizers, and steel fibers, which greatly enhance the mechanical and durability performance of the composite. Silica fume, superplasticizers, and a well-graded aggregate system increase the density of the cementitious matrix, lowering the water-to-cement ratio and reducing internal voids. This densification enhances the overall compactness of the concrete, leading to higher compressive strength and reduced permeability, due to the significant decrease in porosity. Steel fibers, in turn, are incorporated to improve the tensile behavior of UHPC (typically around 15 MPa) by providing distributed reinforcement throughout the matrix. Their inclusion has been shown to substantially enhance the post-cracking performance of the material [CITAR], allowing it to sustain higher loads and larger deformations without brittle failure. Nevertheless, the effectiveness of steel fibers strongly depends on their orientation and dispersion within the cementitious matrix. Undesirable alignment or clustering can significantly limit their contribution, reducing the tensile strength and overall efficiency of UHPC.

Currently, the study of steel fiber behavior relies primarily on experimental methods, where full-scale (1:1) specimens are tested under controlled conditions to analyze fiber orientation under specific circumstances. While valuable, this methodology is highly inefficient: it involves substantial costs, lacks scalability, and does not allow for rapid iteration across multiple variables.

To address these limitations, multiphase Computational Fluid Dynamics (CFD) simulations are proposed as a more effective approach for investigating fiber behavior. Such simulations enable the iterative exploration of both intrinsic UHPC properties—such as rheology—and external factors, including placement techniques, mold geometry, and container dimensions.

To validate the proposed CFD framework, it is necessary to obtain experimental data of UHPC in its fresh state. For this purpose, a Carbopol solution (a transparent, shear-

tunable fluid) will be employed as a substitute for UHPC, allowing controlled experiments to be conducted. Particle Image Velocimetry (PIV), as currently implemented at the university by Cristóbal Maggy and Valentina Tapia, will be used to capture the velocity field of the fluid. In addition, it is essential to analyze how steel fibers behave within the fluid matrix, for which the Particle Tracking Velocimetry (PTV) technique will be self-implemented.

1.1 Hypothesis

Particle concentration can significantly influence the rheological properties of a fluid and, consequently, its flow behavior. This, in turn, affects the final orientation of the particles and thereby the mechanical properties of the composite material (UHPC in this case). It is therefore essential to understand both how individual particles interact with the surrounding fluid and how the collective behavior of the particles modifies the global flow dynamics.

Based on this premise, it is hypothesized that a Discrete Element Method (DEM) coupled with a Computational Fluid Dynamics (CFD) simulation, validated through PIV and PTV techniques, can accurately reproduce the dynamics of particles suspended in a non-Newtonian fluid and, consequently, predict the final orientation of fibers in a UHPC mix.

Such a simulation could be applied to optimize UHPC mix designs, placement techniques, and mold geometries, thereby maximizing the mechanical performance of the final composite material. This approach provides a cost-effective alternative to full-scale experimental testing.

To fully validate this hypothesis, the following objectives are proposed:

1.2 Objectives

1.2.1 General Objective

The general objective of this thesis is to develop a CFD–DEM simulation capable of accurately predicting the dynamics of steel fibers in a Carbopol suspension, validated through PIV and PTV techniques.

1.3 Specific Objectives

To fully achieve the general objective, the following specific objectives are proposed:

- a) Implement a Particle Tracking Velocimetry (PTV) algorithm to analyze the motion of steel fibers in a Carbopol suspension.
- b) Validate the PTV implementation by comparing its results with existing experimental data.
- c) Develop and validate a CFD simulation of a Carbopol suspension, using PIV data for validation.
- d) Integrate a Discrete Element Method (DEM) to simulate the motion of steel fibers within the CFD framework.
- e) Validate the coupled CFD–DEM simulation using PTV data for fiber motion.
- f) Analyze the influence of particle concentration on the rheological properties of the Carbopol suspension and its effect on fiber orientation.
- g) Use the validated CFD–DEM model to predict fiber orientation in various Carbopol mix designs and placement techniques.

1.4 Thesis Structure

AL FINAL PONER TODOS LOS CAPITULOS

Chapter 2

Bibliographic Revision

Throughout this section, a comprehensive review of the literature will be provided. Based on the L-shape model proposed by (Huang, Gao, Li & Wang, 2018) to study UHPC flow dynamics, as illustrated in Figure 2.1 the discussion will focus on the fundamental principles, experimental methodologies, and numerical approaches. Particular emphasis will be placed on Particle Image Velocimetry (PIV) and Particle Tracking Velocimetry (PTV) techniques, along with Discrete Element Method (DEM) and Computational Fluid Dynamics (CFD) frameworks, which together provide the experimental and numerical foundations for analyzing fiber dynamics in viscoplastic media.

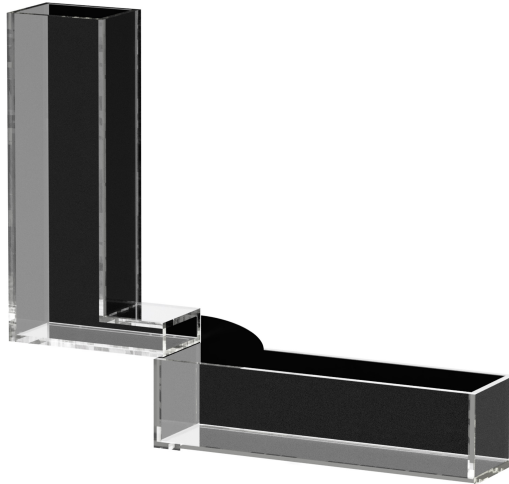


Figure 2.1: L-shape model for UHPC flow analysis
Source: Author's own elaboration.

2.1 Multiphase Flow Simulation

To simulate the behavior of UHPC, a transparent non-Newtonian fluid with tunable rheological properties, known as Carbopol, is employed. As demonstrated by (Auernhammer, Fataei, Haustein, Patel, Schwarze, Secrieru & Mechtcherine, 2020) Carbopol can effectively replicate the flow properties of UHPC. Furthermore, recent work by (Tapia, 2025) has provided a deeper understanding of its behavior under different shear rates and temperatures, offering valuable insights for the simulation process. The rheological properties of Carbopol obtained by Tapia, V. are presented in Figure 2.2 where two concentrations of the fluid (0.2% and 0.5%) were tested.

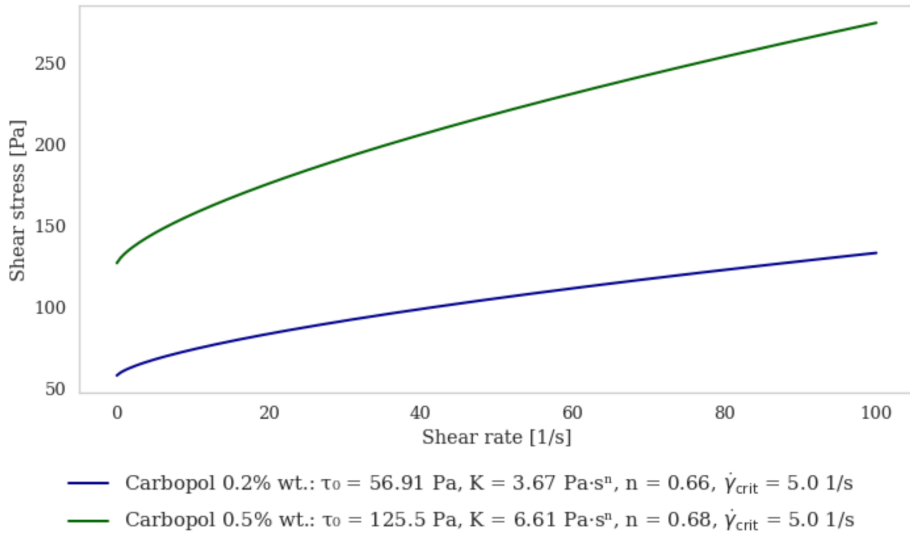


Figure 2.2: Rheological properties of Carbopol at different concentrations
Source: Tapia, V. (2025)

2.1.1 Fluid Phase (CFD)

Computational Fluid Dynamics (CFD) was originally formalized by (Roache, 1972), who emphasized that fluid motion can be described through three fundamental conservation laws: (i) conservation of mass (continuity equation), (ii) conservation of momentum (Newton's second law applied to fluids), and (iii) conservation of energy (first law of thermodynamics applied to fluids). These are expressed as:

$$\frac{\partial \rho}{\partial t} + \nabla \cdot (\rho \mathbf{u}) = 0 \quad (2.1)$$

$$\rho \left(\frac{\partial \mathbf{u}}{\partial t} + \mathbf{u} \cdot \nabla \mathbf{u} \right) = -\nabla p + \mu \nabla^2 \mathbf{u} + \rho \mathbf{g} \quad (2.2)$$

$$\rho \frac{De}{Dt} = -p \nabla \cdot \mathbf{u} + \Phi + \nabla \cdot (k \nabla T) \quad (2.3)$$

Together, these equations form the basis of the Navier-Stokes equations, which govern the motion of fluid substances. For clarity, the same laws can also be expressed in index notation:

$$\frac{\partial \rho}{\partial t} + \frac{\partial(\rho u_i)}{\partial x_i} = 0 \quad (2.4)$$

$$\rho \left(\frac{\partial u_i}{\partial t} + u_j \frac{\partial u_i}{\partial x_j} \right) = -\frac{\partial p}{\partial x_i} + \frac{\partial}{\partial x_j} \left[\mu \left(\frac{\partial u_i}{\partial x_j} + \frac{\partial u_j}{\partial x_i} \right) + \lambda \frac{\partial u_k}{\partial x_k} \delta_{ij} \right] + \rho g_i \quad (2.5)$$

To solve the Navier-Stokes equations across the computational domain, the fluid is discretized into finite volume elements, enabling numerical approximation. The accuracy of this process depends on the shape, size, and arrangement of the elements. Therefore, mesh optimization is crucial to balance accuracy and computational cost, since the Navier-Stokes equations must be solved in every cell (Eymard, Gallouët & Herbin, 2000). Figure 2.3 illustrates a typical CFD computational domain, highlighting two common mesh types used in simulations: tetrahedral and hexahedral elements.

2.1.2 Fiber Phase (DEM)

Based on Newton's laws of motion, the dynamics of a rod-like particle can be expressed as:

$$m \frac{dv}{dt} = \sum F_c + F_d + F_b + mg \quad (2.6)$$

$$I \frac{d\omega}{dt} = \sum T_c \quad (2.7)$$

To simulate the behavior of rod-like particles, a Discrete Element Method (DEM) framework is implemented within a CFD-unresolved simulation. Several analytical approaches have been developed to estimate and detect contacts and forces on non-

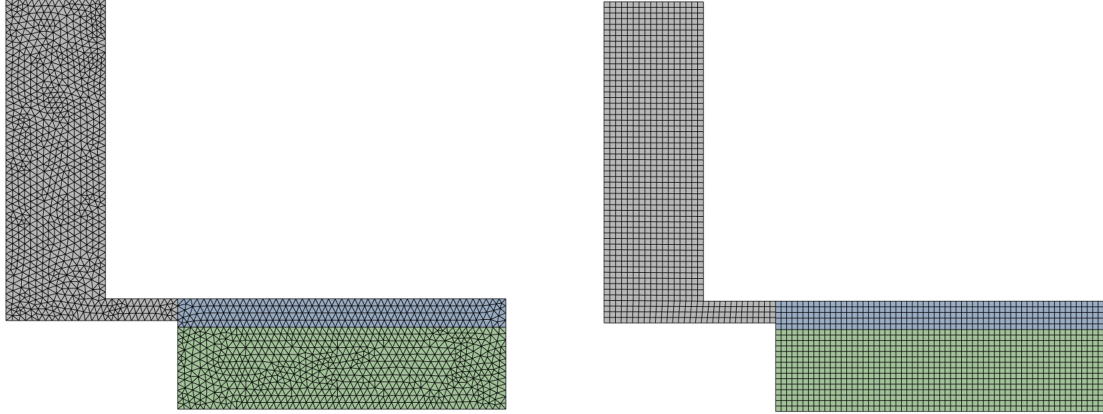


Figure 2.3: Example of a CFD computational domain, with two mesh types: tetrahedrons and hexahedrons.

Source: Author's own elaboration.

spherical particles. For example, (Favier, Abbaspour-Fard, Kremmer & Raji, 1999) proposed representing elongated particles as a cluster of spheres, while (Williams & Pentland, 1992) introduced the use of ellipsoids and superquadrics, defined by:

$$\left(\left| \frac{x}{a} \right|^{s_2} + \left| \frac{y}{b} \right|^{\frac{s_1}{s_2}} \right)^{\frac{s_1}{s_2}} + \left| \frac{z}{c} \right|^{s_1} = 1 \quad (2.8)$$

The general DEM framework proposed by (Cundall & Strack, 1979) reduces particle motion to translational and rotational components, expressed as:

$$m_i \frac{dv_i}{dt} = \sum F_{c,i} + m_i g + f_{pf,i} \quad (2.9)$$

$$\frac{d(I_i \omega_i)}{dt} = R_i \cdot (\sum M_{c,i} + M_{pf,i}) \quad (2.10)$$

Different approaches have been proposed to couple the fluid and fiber phases. Among them, one-way and two-way coupling methodologies are commonly used to simulate multiphase flows, in which the fluid phase is solved using CFD and the particle phase using DEM.

2.1.3 Phases Coupling (CFD-DEM)

In one-way coupling, the fluid influences particle motion, but the particles do not affect the fluid flow. This approach is suitable for dilute systems where particle-particle interactions are negligible. In contrast, two-way coupling accounts for the mutual interaction between the fluid and the particles, making it more appropriate for dense systems in which particle concentration significantly modifies the flow dynamics (Guzman, Chen & Landry, 2023).

Commercially, ANSYS provides specialized tools for such simulations, with Fluent used to solve the fluid phase and Rocky employed to model the discrete phase.

One-Way Coupling

In the one-way coupling regime (dilute suspensions, $\alpha_p \ll 1$), the fluid phase evolves independently of the particles (no feedback), while particles feel the fluid through hydrodynamic forces. The fluid equations reduce to the standard Navier-Stokes system without interphase source terms:

$$\frac{\partial \rho_f}{\partial t} + \nabla \cdot (\rho_f \mathbf{u}_f) = 0, \quad (2.11)$$

$$\rho_f \left(\frac{\partial \mathbf{u}_f}{\partial t} + \mathbf{u}_f \cdot \nabla \mathbf{u}_f \right) = -\nabla p + \nabla \cdot \boldsymbol{\tau}_f + \rho_f \mathbf{g}, \quad \boldsymbol{\tau}_f = \mu [\nabla \mathbf{u}_f + (\nabla \mathbf{u}_f)^T] + \lambda (\nabla \cdot \mathbf{u}_f) \mathbf{I}. \quad (2.12)$$

Each particle p is advanced in Lagrangian form by:

$$m_p \frac{d\mathbf{u}_p}{dt} = \mathbf{F}_p^{\text{hyd}} + m_p \mathbf{g} + \sum \mathbf{F}_p^c, \quad \mathbf{x}'_p = \mathbf{u}_p, \quad (2.13)$$

$$\mathbf{I}_p \frac{d\boldsymbol{\omega}_p}{dt} = \mathbf{T}_p^{\text{hyd}} + \sum \mathbf{T}_p^c, \quad (2.14)$$

where $\mathbf{F}_p^{\text{hyd}}$ and $\mathbf{T}_p^{\text{hyd}}$ collect hydrodynamic interactions (e.g., drag, buoyancy, pressure-gradient, lift, added mass) evaluated from the local fluid field (ρ_f , \mathbf{u}_f , p), and $\sum \mathbf{F}_p^c$, $\sum \mathbf{T}_p^c$ are contact forces/torques from DEM (collisions, friction, etc.). No momentum is fed back to the fluid in this regime:

$$\mathbf{S}_m(\mathbf{x}, t) = \mathbf{0}.$$

Two-Way Coupling

In the two-way coupling regime (moderate to dense suspensions), particles exchange momentum and energy with the fluid. The fluid equations include porosity $\alpha_f = 1 - \alpha_p$ and interphase source terms:

$$\frac{\partial(\alpha_f \rho_f)}{\partial t} + \nabla \cdot (\alpha_f \rho_f \mathbf{u}_f) = 0, \quad (2.15)$$

$$\frac{\partial(\alpha_f \rho_f \mathbf{u}_f)}{\partial t} + \nabla \cdot (\alpha_f \rho_f \mathbf{u}_f \mathbf{u}_f) = -\alpha_f \nabla p + \nabla \cdot (\alpha_f \boldsymbol{\tau}_f) + \alpha_f \rho_f \mathbf{g} + \mathbf{S}_m, \quad (2.16)$$

The momentum source \mathbf{S}_m is the volumetric feedback from particles to the fluid. In discrete form, for a control volume (cell) c of volume V_c :

$$\mathbf{S}_{m,c}(t) = -\frac{1}{V_c} \sum_{p \in c} \mathbf{F}_p^{\text{hyd}}(t), \quad (2.17)$$

The particle updates remain Lagrangian but now the same hydrodynamic forces that accelerate particles are *exactly* returned to the fluid with opposite sign:

$$m_p \frac{d\mathbf{u}_p}{dt} = \mathbf{F}_p^{\text{hyd}} + m_p \mathbf{g} + \sum \mathbf{F}_p^c, \quad \mathbf{I}_p \frac{d\boldsymbol{\omega}_p}{dt} = \mathbf{T}_p^{\text{hyd}} + \sum \mathbf{T}_p^c, \quad (2.18)$$

$$\alpha_{p,c} = \frac{1}{V_c} \sum_{p \in c} V_p, \quad \alpha_{f,c} = 1 - \alpha_{p,c}, \quad (2.19)$$

where V_p is the volume of the particle (or fiber), and $\alpha_{p,c}$ is the volume fraction in cell c .

To validate both fluid and particle motion, non-intrusive experimental methodologies have been developed such as PIV for capturing velocity fields and PTV for resolving particle trajectories.

2.2 Particle Image Velocimetry

Particle Image Velocimetry (PIV) is an optical flow visualization technique used to obtain instantaneous velocity measurements and related properties in fluids, enabling the reconstruction of Eulerian velocity fields (Raffel, Willert, Scarano, Kähler, Wereley & Kompenhans, 2018) through image correlation methods. The fluid is seeded with

tracer particles that are assumed to accurately follow the flow dynamics. These particles are illuminated by a laser sheet, as shown in Figure 2.4 which presents the setup implemented by (Maggi, 2023) at Universidad de los Andes. The particle motion is captured using a high-speed camera, and the recorded images are subsequently analyzed to determine the velocity field of the fluid.

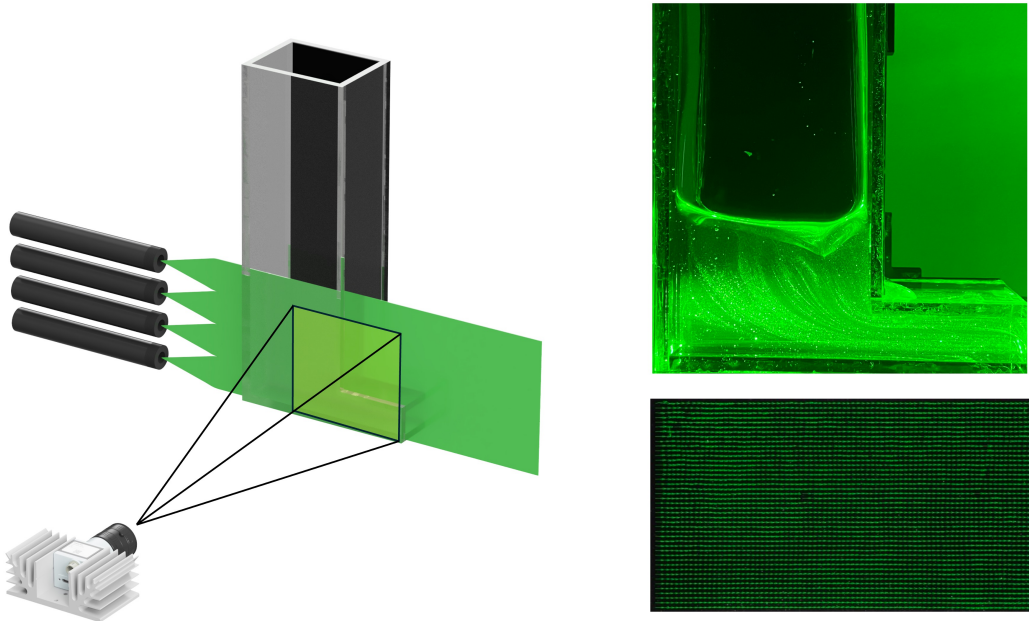


Figure 2.4: PIV setup based on the L-Shape model
Source: Author's own elaboration.

2.3 Particle Tracking Velocimetry

While PIV enables the study of Eulerian velocity fields, Particle Tracking Velocimetry (PTV) provides a Lagrangian perspective, resolving the motion of individual particles with high temporal resolution (Maas, Gruen & Papantoniou, 1993).

Although PIV used an illuminated plane to capture the motion of particles, PTV requires a volumetric approach to accurately track the three-dimensional trajectories and rotation of particles. Thus, and based on the PIV setup, volumetric illumination LEDs were used to capture the motion of particles within a defined volume, as Figure 2.5 shows.

Since PTV must be self-implemented for this work, a more detailed literature review was

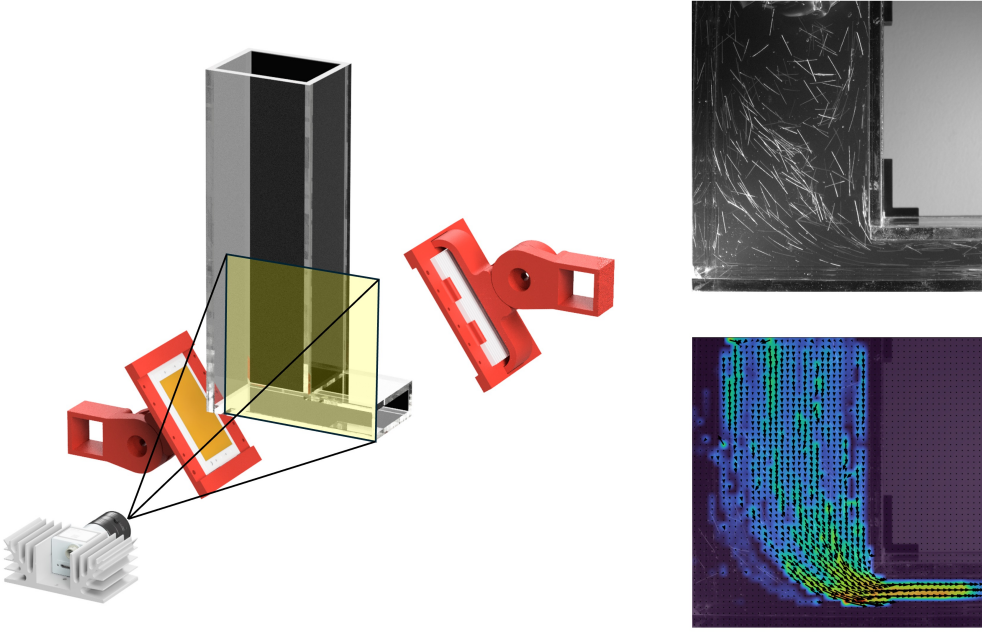


Figure 2.5: PTV setup based on volumetric illumination
Source: Author's own elaboration.

conducted, with particular emphasis on particle detection and tracking methodologies.

2.3.1 Particle Detection

Several methodologies have been developed for particle detection in PTV, ranging from traditional computational algorithms such as the Hough Transform, Canny filtering, and edge detection, as reviewed in (Seyfi, Karimpour & Balachandar, 2024) to more recent approaches based on deep learning, which have demonstrated superior reliability compared to classical methods (Plaksyvyi, Skublewska-Paszkowska & Powroźnik, 2023). In particular, segmentation models have shown strong robustness and performance, as reported by (Qamar, Baba, Verger & Andersson, 2024) where a YOLO-based model was successfully applied to small rod-like particles. Throughout this work, conventional algorithms are compared with deep learning-based models to assess their effectiveness in detecting and tracking UHPC fibers in a viscoplastic medium.

The performance of these detection methodologies is often evaluated using confusion matrices, which provide a comprehensive overview of the model's predictive capabilities. These matrices summarize the counts of true positives (TP), false positives (FP), true negatives (TN), and false negatives (FN), allowing for the calculation of key metrics

such as precision, recall, F1-score and Intersection over Union (IoU) as (Everingham, Eslami, Van Gool, Williams, Winn & Zisserman, 2015) defined:

$$\text{Precision} = \frac{TP}{TP + FP} \quad (2.20)$$

$$\text{Recall} = \frac{TP}{TP + FN} \quad (2.21)$$

$$\text{F1 Score} = 2 \cdot \frac{\text{Precision} \cdot \text{Recall}}{\text{Precision} + \text{Recall}} \quad (2.22)$$

$$\text{IoU} = \frac{TP}{TP + FP + FN} \quad (2.23)$$

2.3.2 Particle Correlation

Once particles are detected, they need to be linked across consecutive frames. Based on the characteristics and motion of each rod-like particle, it becomes possible to reliably identify and track individual fibers over time. Several tracking methods have been developed for this purpose, including nearest-neighbor approaches, Kalman filtering, and more advanced deep learning-based techniques. In the present work, an α - β - γ filter (Tenne & Singh, 2000) and (Gray & Murray, 1993) derived from the Kalman filter (Welch, Bishop & others, 1995) was implemented. This filter uses the known state of an object Z_n (position, velocity, and acceleration) together with a prediction-correction scheme to estimate its future state, based on the present state $\hat{X}_{n,n-1}$, while continuously updating the prediction by incorporating new measurements. This approach allows for robust tracking of fibers even in the presence of noise or partial occlusions.

$$\hat{X}_{n,n-1} = \hat{X}_{n-1,n-1} + K_n \cdot (Z_n - \hat{X}_{n,n-1}) \quad (2.24)$$

K_n is known as Kalman gain, which determines the weight given to the new measurement versus the prediction. The filter parameters α , β , and γ control the responsiveness of the filter to changes in position, velocity, and acceleration, respectively both lineal and angular movements:

$$\hat{X}_{n,n-1} = \hat{X}_{n-1,n-1} + \alpha \cdot (Z_n - \hat{X}_{n,n-1}) \quad (2.25)$$

$$\dot{\hat{X}}_{n,n-1} = \dot{\hat{X}}_{n-1,n-1} + \beta \cdot (Z_n - \hat{X}_{n,n-1}) / \Delta t \quad (2.26)$$

$$\ddot{\hat{X}}_{n,n-1} = \ddot{\hat{X}}_{n-1,n-1} + \gamma \cdot (Z_n - \hat{X}_{n,n-1}) / (2 \cdot \Delta t^2) \quad (2.27)$$

Then, it is necessary update the model to time variation between each frame, as all the variables experience a change, basic dynamic equation should be applied to obtain the corresponding data as the followings equations show:

$$\hat{X}_{n,n} = \hat{X}_{n,n-1} + \dot{\hat{X}}_{n,n-1} \cdot \Delta t + \frac{1}{2} \cdot \ddot{\hat{X}}_{n,n-1} \cdot \Delta t^2 \quad (2.28)$$

$$\dot{\hat{X}}_{n,n} = \dot{\hat{X}}_{n,n-1} + \ddot{\hat{X}}_{n,n-1} \cdot \Delta t \quad (2.29)$$

$$\ddot{\hat{X}}_{n,n} = \ddot{\hat{X}}_{n,n-1} \quad (2.30)$$

Therefore, it is possible to take the current fiber parameters and use them as input for the α - β - γ filter for each fiber, where $\Delta t = 1/fps$. This will output a virtual fiber corresponding to each fiber recognized in the previous frame. The virtual fiber that satisfies all the criteria will be linked to the newly detected fiber. Additionally, when each particle is first detected, the initial linear and angular velocity and the acceleration are assumed to be zero, regardless of the time instant.

Chapter 3

Methodology

3.1 Particle Tracking Velocimetry Implementation

PTV is typically structured into three main steps, as illustrated in Figure 3.1: (i) particle detection, (ii) particle characterization, and (iii) particle tracking. Following these stages, a post-processing step is performed to refine the results and enhance the quality of the data analysis.

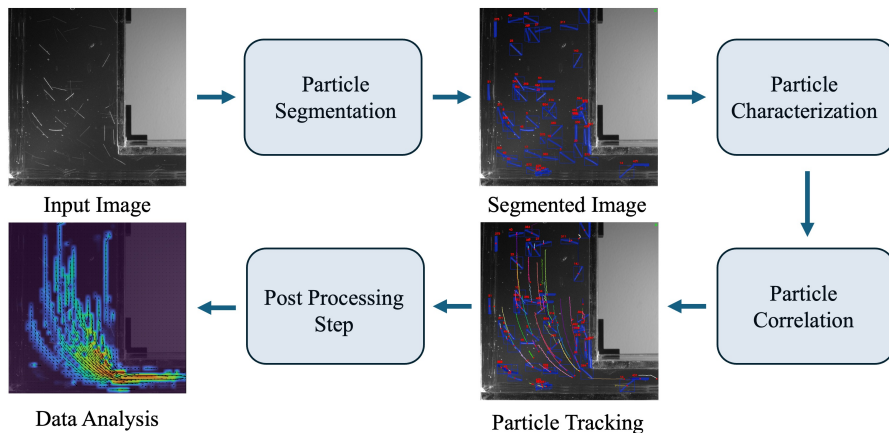


Figure 3.1: PTV flowchart
Source: Author's own elaboration.

Since UHPC fibers often exhibit non-uniform surface properties, the light they reflect may vary along their length or be affected by suboptimal alignment with respect to the light source (see Figure 3.2). Consequently, conventional detection methods proved inadequate. To overcome this limitation, deep learning-based approaches were tested, as the literature has demonstrated their effectiveness in detecting small rod-like particles.

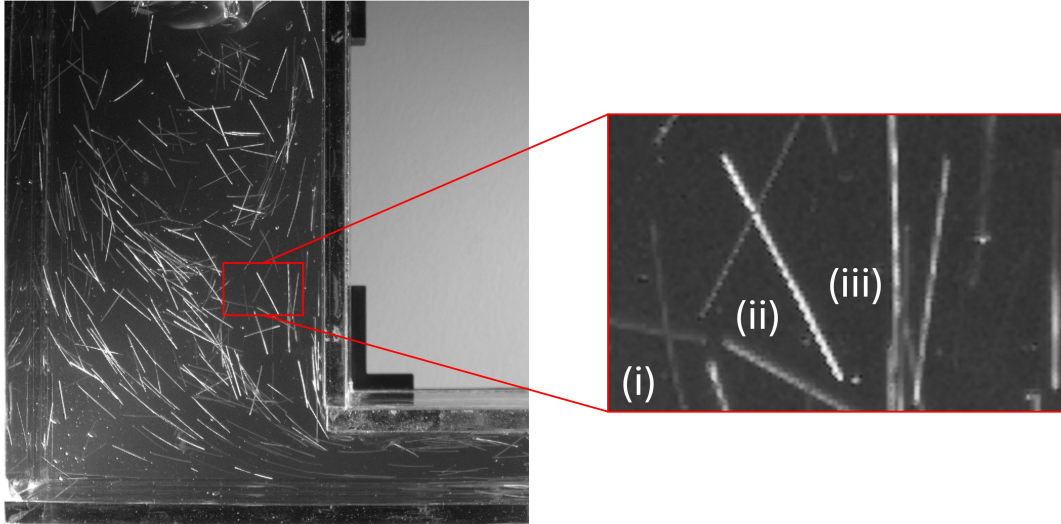


Figure 3.2: Examples of fiber light reflection: (i) a group of fibers with suboptimal alignment relative to the light source, (ii) a well-illuminated fiber, and (iii) a fiber exhibiting non-uniform light reflection along its length.

Source: Author's own elaboration.

The Hough Transform was compared with YOLOv11 and SAM2 to evaluate their performance in detecting and tracking UHPC fibers. Both YOLO and SAM were trained using the same dataset, which consisted of two sets of images: (i) a low-density case with few fibers and no overlapping, and (ii) a high-density case with a larger number of fibers and overlapping, as Figure 3.3 shows.

The results showed that the Hough Transform achieved low detection accuracy. Although some fibers were correctly identified as true positives (TP), the method also produced a high number of false positives (FP). In contrast, YOLOv11 demonstrated high precision, successfully detecting overlapping fibers while maintaining a low FP rate, as evidenced by the confusion matrix in Figure REFERENCIAR. Finally, SAM2 failed to produce any valid detections, resulting in all evaluation metrics being zero, as

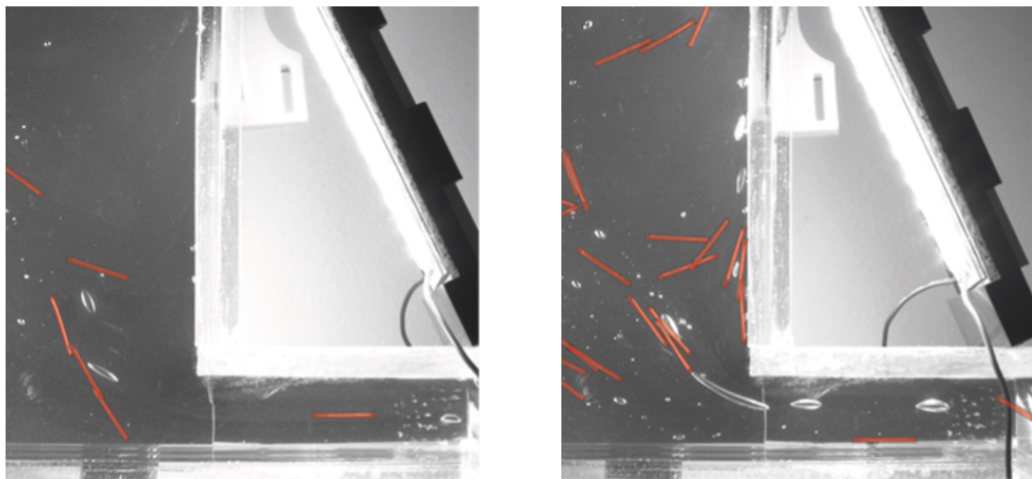


Figure 3.3: Representative examples from the training dataset: (a) image with a low concentration of well-separated fibers; (b) image with a high concentration of overlapping fibers and a significant presence of bubbles.

Source: Author's own elaboration.

summarized in Table REFERENCIAR.

Nomenclature

Bibliography

- Auernhammer, G. K., Fataei, S., Haustein, M. A., Patel, H. P., Schwarze, R., Secrieru, E., & Mechtkerine, V. (2020). Transparent model concrete with tunable rheology for investigating flow and particle-migration during transport in pipes. *Materials & Design*, 193, 108673.
- Cheng, D., Reiner, D. M., Yang, F., Cui, C., Meng, J., Shan, Y., Liu, Y., Tao, S., & Guan, D. (2023). Projecting future carbon emissions from cement production in developing countries. *Nature Communications*, 14(1), 8213.
- Cundall, P. A. & Strack, O. D. (1979). A discrete numerical model for granular assemblies. *geotechnique*, 29(1), 47–65.
- Everingham, M., Eslami, S. A., Van Gool, L., Williams, C. K., Winn, J., & Zisserman, A. (2015). The pascal visual object classes challenge: A retrospective. *International journal of computer vision*, 111(1), 98–136.
- Eymard, R., Gallouët, T., & Herbin, R. (2000). Finite volume methods. *Handbook of numerical analysis*, 7, 713–1018.
- Favier, J. F., Abbaspour-Fard, M. H., Kremmer, M., & Raji, A. O. (1999). Shape representation of axi-symmetrical, non-spherical particles in discrete element simulation using multi-element model particles. *Engineering computations*, 16(4), 467–480.
- Gray, J. & Murray, W. (1993). A derivation of an analytic expression for the tracking index for the alpha-beta-gamma filter. *IEEE Transactions on Aerospace and Electronic Systems*, 29(3), 1064–1065.
- Guzman, L., Chen, Y., & Landry, H. (2023). Coupled cfd-dem simulation of seed flow in horizontal-vertical tube transition. *Processes*, 11(3), 909.
- Huang, H., Gao, X., Li, L., & Wang, H. (2018). Improvement effect of steel fiber orientation control on mechanical performance of uhpc. *Construction and Building Materials*, 188, 709–721.

- Maas, H.-G., Gruen, A., & Papantoniou, D. (1993). Particle tracking velocimetry in three-dimensional flows: Part 1. photogrammetric determination of particle coordinates. *Experiments in fluids*, 15(2), 133–146.
- Maggi, C. A. (2023). Sistema de velocimetría de imágenes de partículas. Trabajo de titulación para optar al título de ingeniero civil eléctrico, Universidad de los Andes, Santiago, Chile. Profesor Guía: Gustavo Luis Funes.
- Plaksyvyi, A., Skublewska-Paszkowska, M., & Powroźnik, P. (2023). A comparative analysis of image segmentation using classical and deep learning approach. *Advances in Science and Technology Research Journal*, 17(6), 127–139.
- Qamar, S., Baba, A., Verger, S., & Andersson, M. (2024). Segmentation and characterization of macerated fibers and vessels using deep learning. arxiv. *arXiv preprint arXiv:2401.16937*.
- Raffel, M., Willert, C. E., Scarano, F., Kähler, C. J., Wereley, S. T., & Kompenhans, J. (2018). *Particle image velocimetry: a practical guide*. Springer.
- Roache, P. J. (1972). *Computational Fluid Dynamics*. Albuquerque, NM: Hermosa Publishers.
- Seyfi, S., Karimpour, S., & Balachandar, R. (2024). Simultaneous flow and particle measurements for multiphase flows in hydraulic engineering: A review and synthesis of current state. *Flow Measurement and Instrumentation*, 99, 102666.
- Tapia, V. A. (2025). Experimental analysis of fiber-fluid dynamics in viscoplastic media using piv. Trabajo de titulación para optar al título de magister en ciencias de la ingeniería, Universidad de los Andes, Santiago, Chile. Profesor Guía: Patricio Moreno.
- Tenne, D. & Singh, T. (2000). Optimal design of α - β - γ filters. *Proceedings of the American Control Conference*, 6, 4348 – 4352 vol.6.
- Welch, G., Bishop, G., et al. (1995). An introduction to the kalman filter.
- Williams, J. R. & Pentland, A. P. (1992). Superquadrics and modal dynamics for discrete elements in interactive design. *Engineering Computations*, 9(2), 115–127.

Winnefeld, F., Leemann, A., German, A., & Lothenbach, B. (2022). Co₂ storage in cement and concrete by mineral carbonation. *Current Opinion in Green and Sustainable Chemistry*, 38, 100672.